

# Bioinspired binary-site catalysts for novel urea-assisted Zn-air battery: A transfer station between renewable energy and hydrogen

Wen-Wen Tian, Jin-Tao Ren, Hao-Yu Wang, Lei Wang, Zhong-Yong Yuan<sup>\*</sup>

School of Materials Science and Engineering, Smart Sensing Interdisciplinary Science Center, Nankai University, Tianjin 300350, China

## ARTICLE INFO

### Keywords:

Biomimetic design  
Urea-assisted Zn-air battery  
Oxygen reduction reaction  
Urea oxidation reaction  
Built-in electric field

## ABSTRACT

The slow reaction kinetics of oxygen electrode is the bottleneck restricting the development of rechargeable Zn-air batteries (ZABs). In order to further improve the energy conversion efficiency of ZABs, a novel urea-assisted ZAB system was proposed by replacing oxygen evolution reaction (OER) with urea oxidation reaction (UOR) with lower theoretical thermodynamic potential. Inspired by nature's ingenious structure-function, a "leaf-branch" CoNi@NCNTs-LDH/CC binary-site electrocatalyst was designed for the above system, where spatially separated branches and leaves serve as the main active sites for ORR and UOR, respectively. A built-in electric field from CoNi-LDH to CoNi@NCNTs is formed at the interface of the composite, which plays a command effect, effectively triggering the accumulation of O<sub>2</sub> and urea reactants around the CoNi and LDH sites, respectively, and thus improving the efficiency of both ORR and UOR reactions. Based on that, a conceptual urea-assisted rechargeable ZAB is demonstrated to have significantly decreased charging voltage, higher energy conversion efficiency (74.6 %) compared with the conventional ZAB, as well as high urea elimination rates. Considering the urea-assisted ZAB with high energy conversion efficiency and wastewater treatment versatility as an energy transfer station applied in a high value-added agricultural system, uninterrupted hydrogen production and wastewater treatment of agricultural wastewater can be simultaneously achieved using sustainable energy sources.

## 1. Introduction

The growing demand for energy and power in modern society has driven the rapid development of sustainable and high-efficiency energy conversion and storage technologies [1,2]. Rechargeable Zn-air batteries (ZABs), with the advantages of high theoretical energy density, low cost, favorable environmental compatibility, and impressive security, have a broad application prospect in the field of power grid energy storage [3–5]. Nevertheless, there are critical challenges for the development of reversible ZABs, where the sluggish reaction kinetics for oxygen reduction (ORR) and evolution reaction (OER) in air cathode with large overpotentials severely limits the energy conversion efficiency [6,7]. To this end, on the one hand, high-efficiency bifunctional oxygen electrode catalysts are highly desired, to accelerate ORR/OER kinetics and reduce oxygen reaction overpotentials, for decreasing the voltage gap during the discharging and charging process of ZABs [8]. On the other hand, it has been reported that some small molecules (urea, hydrazine, carbohydrates, alcohol, etc.) oxidation reactions are thermodynamically more favorable than OER in the alkaline electrolyte system

[9–11]. Hence, directly replacing anodic OER (0.40 V vs. SHE) by the above oxidation reactions with more favorable kinetics and lower reaction overpotentials will provide another opportunity to decrease the charging voltage and improve the utilization efficiency of ZABs. Among them, urea oxidation reaction (UOR) is an attractive alternative, with a low theoretical thermodynamic potential (-0.46 V vs. SHE) and abundant sources, as urea exists in the usual pollutants from industrial and agricultural wastewater [12,13]. In contrast to the OER process in conventional rechargeable ZABs, the charging cycle in urea-assisted ZABs is different and can be performed more easily. Theoretically, the constructed urea-assisted ZABs can be charged at a reduced voltage of 0.79 V (Fig. 1a), much lower than that of conventional rechargeable ZABs (1.65 V) [9]. Thus, through coupling ORR and UOR to construct urea-assisted rechargeable ZAB (Fig. 1b), can not only improve the charging property and overall energy conversion efficiency of ZAB, but also provide a potential way for removing urea from urea-rich wastewater, achieving high energy efficiency and pollutants degradation at the same time.

To assure the efficient and reliable operation of urea-assisted ZABs,

<sup>\*</sup> Corresponding author.

E-mail address: [zyyuan@nankai.edu.cn](mailto:zyyuan@nankai.edu.cn) (Z.-Y. Yuan).

<https://doi.org/10.1016/j.apcatb.2024.124115>

Received 1 March 2024; Received in revised form 17 April 2024; Accepted 22 April 2024

Available online 23 April 2024

0926-3373/© 2024 Elsevier B.V. All rights reserved.



advanced bi-functional electrocatalysts with high ORR and UOR activity and stability are essential. Currently, precious metal Pt-based catalysts are identified as superior electrocatalysts for ORR, while Ir- and Ru-based catalysts are efficient for OER/UOR in alkaline media, but the scarcity, high cost and unsatisfactory stability limit the large-scale implementations [14–16]. Various non-precious metal electrocatalysts have then been investigated as the potential alternatives. It is widely believed that transition metal-based materials (transition metals, carbides, nitrides, etc.), transition metal-nitrogen-carbon materials (M-N<sub>x</sub>/C) and carbon materials exhibit promising ORR activity [17–19]. It has also been demonstrated that more attractive properties than single-metal catalysts can be achieved by deliberately introducing bimetallic or multimetallic sites with improved chemical and electronic properties and synergistic effects [20–23]. While layered double hydroxides (LDHs), phosphides and sulfides are beneficial to catalyze OER/UOR [24,25]. Furthermore, catalysts with Ni-rich sites have also been demonstrated to have significant UOR electrocatalytic activity [9, 26,27]. Taking consideration of the different mechanisms of ORR and UOR and the requirement for different active sites, the combination strategy integrating two or more types of components for ORR/UOR electrocatalysts would offer the possibility to select their respective active sites. And, how to carry out the catalyst nanostructure design to protect different sites to maximize their respective roles without interfering with each other and synergistically improve the overall bifunctional activity of the catalyst will be the key and difficult point.

In nature, green plants flourish and grow vigorously, accompanied by efficient photosynthesis, thanks to the fact that different organs of the plant body are independent in their division of duties, but are coordinated with each other and work closely together to accomplish a variety of complex life activities. In this regard, inspired by the cooperation of plant branches and leaves during photosynthesis, it is instructive to design catalyst structures with binary active sites. Scheme 1 is a partial structure-function diagram of the life activity of the green plant, displaying the cooperative relationship between the two sites of the branches and leaves. The luxuriant leaves grow sequentially onto the branches in order and are exposed in large areas for better light utilization, where the conversion of carbon dioxide and water to organic matter is completed, which serve as the major sites for nutrient production. In addition, the continuous growth of the plant depends on the supply of branches, which are considered as the primary sites for nutrient stores. Note how the two sites are connected and closely coordinated to facilitate the implementation of their respective functions, while simultaneously performing nutrient production and storage. This is mainly related to the duct-sieve cells at the junctions of the branches

and leaves, which selectively exchange substances through the cell membrane, driven by osmotic pressure. The reactants of photosynthesis, water and inorganic salts, are transported from the branches to the leaves from the bottom up, while the products of photosynthesis, organic matter, are transported from the leaves to the branches from the top down. As a result, the leaves deliver nutrients for the growth of the branches, which in turn act as a substrate for the leaves and provide support and stability, thereby promoting the joint prosperity of the branches and the leaves. Branches and leaves are complementary, interdependent and mutually reinforcing, forming an organic whole.

In this work, inspired by nature's ingenious structure-function, we herein demonstrate a binary-site "leaf-branch" catalyst design of CoNi@NCNTs-LDH/CC for specific ORR-UOR electrocatalytic process, and the relationship between the two sites was explored. For the CoNi@NCNTs-LDH/CC composite catalyst, the CoNi@NCNTs serve as branches and ultra-thin nanosheets (CoNi-LDH) serve as leaves, which provides reaction sites for ORR and UOR, respectively, ensuring the high efficiency at respective sites, and also complementing each other in structure, providing suitable reaction microenvironment for the two reactions. At the same time, inspired by the exchange of materials in different organs of branches and leaves, it was found that an internal electric field from CoNi-LDH to CoNi@NCNTs was formed at the interface of the composite. The DFT theoretical calculation proves that CoNi sites are favorable for the adsorption of O<sub>2</sub> reactants during ORR process, while urea molecules have a stronger trend to be adsorbed at LDH sites during UOR process, which induces a "command effect", promoting the enrichment of reaction substrates to their respective reaction sites and further endowing the CoNi@NCNTs-LDH/CC with efficient ORR and UOR catalytic activity. Based on CoNi@NCNTs-LDH/CC, the urea-assisted ZAB batteries exhibit lower charging voltage, smaller voltage gap (0.43 V) and higher energy conversion efficiency (74.6 %) compared with conventional ZAB batteries, and can keep over 350 h of stable operation. Additionally, a urea elimination rate of 78.9 g m<sup>-2</sup> h<sup>-1</sup> is synchronously achieved during the battery charging process. The urea-assisted ZAB is then considered as a high-efficiency transfer station to further drive urea-assisted water splitting system, achieving efficient H<sub>2</sub> generation from agricultural wastewater only utilizing sustainable energy sources, and simultaneous agricultural wastewater purification.

## 2. Experimental section

### 2.1. Synthesis of (Co,Ni)(CO<sub>3</sub>)<sub>0.5</sub>OH/CC

(Co,Ni)(CO<sub>3</sub>)<sub>0.5</sub>OH nanowire arrays were synthesized on carbon

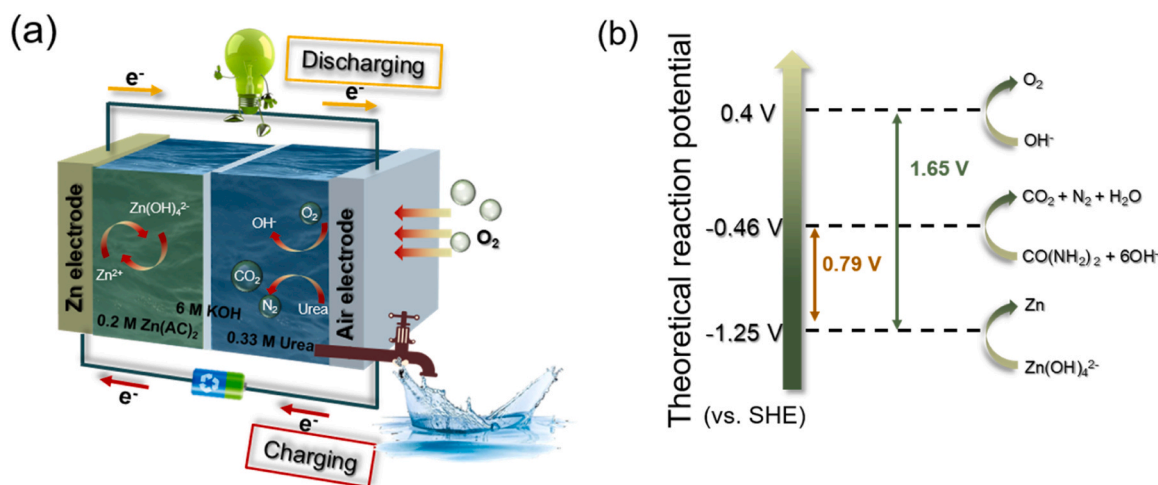
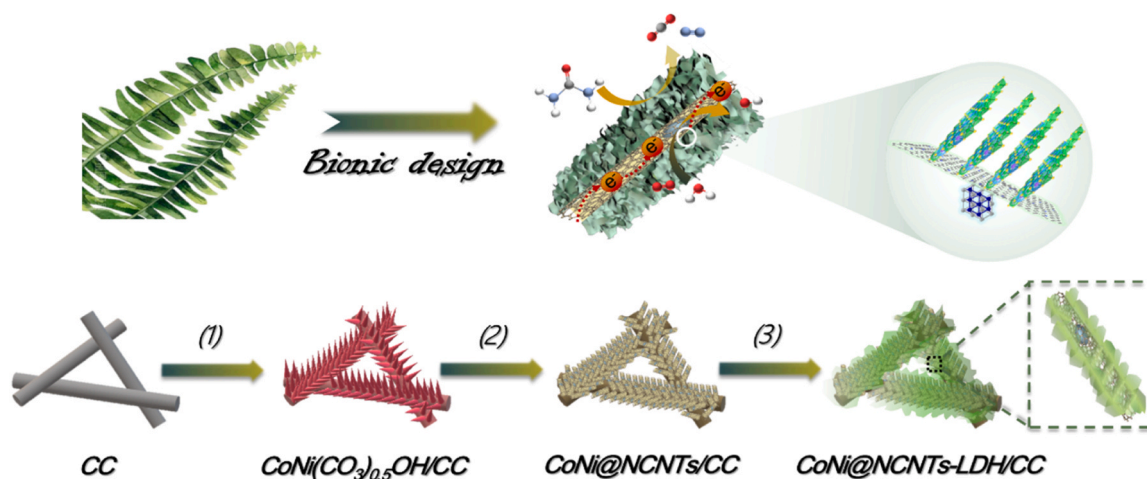


**Fig. 1.** (a) Schematic illustration of charging and discharging process for urea-assisted rechargeable ZABs. (b) Comparison of the theoretical charging voltages of urea-assisted and conventional ZABs.





**Scheme 1.** Schematic showing the bionic design and synthetic process of CoNi@NCNTs-LDH/CC.

cloth (CC) substrate by typical hydrothermal deposition. Prior to hydrothermal deposition, the cleaned CC was treated with 68 %  $\text{HNO}_3$  solution at room temperature for 4 h, then was repeatedly washed with deionized water and dried. In a typical process, 4.8 mmol  $\text{CoCl}_2 \cdot 6 \text{H}_2\text{O}$ , 2.4 mmol  $\text{NiCl}_2 \cdot 6 \text{H}_2\text{O}$ , as well as 12 mmol urea were dissolved in 40 mL deionized water under continuous agitation. Then, the homogeneous solution was transferred to a 50 mL Teflon-lined stainless steel autoclave, with the acid-treated CC immersed in it, and kept at 120 °C for 6 h. After cooling down to room temperature, the  $(\text{Co,Ni})(\text{CO}_3)_{0.5}\text{OH}$  nanowire array precursor grown on CC was obtained by washing with deionized water and drying, which is named  $(\text{Co,Ni})(\text{CO}_3)_{0.5}\text{OH/CC}$ .

## 2.2. Synthesis of CoNi@NCNTs/CC

In general, the prepared  $(\text{Co,Ni})(\text{CO}_3)_{0.5}\text{OH/CC}$  ( $2 \times 4 \text{ cm}^2$ ) and 1.5 g  $\text{g-C}_3\text{N}_4$  were put into the same porcelain boat in a tubular furnace, heated at 800 °C for 3 h at a heating rate of  $5 \text{ °C min}^{-1}$  in  $\text{N}_2$  atmosphere. After calcination, the  $(\text{Co,Ni})(\text{CO}_3)_{0.5}\text{OH}$  nanowire array precursor was transformed into nanotube array embedded with CoNi nanoparticles, which is named CoNi@NCNTs/CC.

## 2.3. Synthesis of CoNi@NCNTs-LDH/CC

The as-synthesized CoNi@NCNTs/CC was used as the skeletons for the growth of CoNi-LDH nanosheets by electrodeposition method, and the resulted sample was named CoNi@NCNTs-LDH/CC. In the electrodeposition process, 0.204 g  $\text{Co}(\text{NO}_3)_2 \cdot 6 \text{H}_2\text{O}$  and 0.204 g  $\text{Ni}(\text{NO}_3)_2 \cdot 6 \text{H}_2\text{O}$  were uniformly dispersed in deionized water, served as the electrolyte. A piece of CoNi@NCNTs/CC was used directly as the working electrode, with the graphitic rod and Ag/AgCl as the counter electrode and reference electrode, respectively. The samples with different deposition time of 100, 300 and 500 s were prepared, named CoNi@NCNTs-LDH/CC- $x$  ( $x$  represents the deposition time). The samples were then washed with deionized water to remove electrolyte ions and dried in an oven at 80 °C for 6 h.

## 2.4. Synthesis of CoNi-LDH/CC

For the comparison, CoNi-LDH/CC was prepared, through the electrodeposition process similar to CoNi@NCNTs-LDH/CC, except that the working electrode was replaced with a piece of CC.

Other details of physical characterization, electrochemical measurements and DFT calculations are provided in the [Supporting Information \(SI\)](#).

## 3. Results and discussion

### 3.1. Synthesis and characterizations

Inspired by the cooperation of plant branches and leaves during photosynthesis, a similar binary-site catalyst structure design of an ideal "leaf-branch" electrocatalyst was proposed for the urea-assisted ZAB system. Based on the concept, a CoNi@NCNTs-LDH composite is constructed, in which the "leaf" of thin layered double hydroxides (LDH) is grown directly on the "branch" of carbon nanotube, with two components joining together to support each other. The synthesis process is shown in [Scheme 1](#). With the treated CC ([Fig. S1](#)) as the substrate, the  $\text{CoNi}(\text{CO}_3)_{0.5}\text{OH/CC}$  precursor with nanowire array structure ([Fig. S2](#)) was prepared through the hydrothermal method. After calcination, the precursor nanowires transformed into CoNi alloys derived NCNTs arrays (CoNi@NCNTs/CC), where large amounts of nanotubes extend outward from the substrate of CC ([Fig. S3](#)). Afterwards, CoNi@NCNTs are treated as "branches" to grow layered double hydroxides as dense leaves by the electrodeposition method, to obtain the resultant CoNi@NCNTs-LDH/CC catalysts (under electrodeposition operation for 300 s). The crystalline structure of the obtained composite was determined by X-ray diffraction (XRD) measurements ([Fig. S4](#)). Besides the relative intense peak at  $2\theta = 44.3^\circ$ ,  $51.6^\circ$  and  $76.0^\circ$  ascribed to the (111), (200) and (220) planes of CoNi alloy component, the other inconspicuous peaks located at  $2\theta = 11.6^\circ$ ,  $23.1^\circ$ ,  $34.9^\circ$ ,  $39.4^\circ$ ,  $60.9^\circ$  and  $62.4^\circ$  are identified as the (003), (006), (012), (015), (110) and (113) lattice planes of the hydrotalcite-like CoNi-LDH phase [28], demonstrating the successful construction of CoNi-LDH phase on the basis of the carbon tubes encapsulating the CoNi alloys.

The morphology of the CoNi@NCNTs-LDH/CC composite was investigated by field emission scanning electron microscopy (SEM) and transmission electron microscopy (TEM). SEM images at different magnifications are shown in [Fig. 2a-d](#), where the dense branches of carbon nanotubes extend outward from the carbon fiber of the CC, and the outer wall of each carbon nanotube is distributed with radially grown nanosheets, forming a decentralized and ordered array structure. A large number of ultrathin CoNi-LDH nanosheets are grown directly on the surface of CoNi@NCNTs in a vertical orientation, effectively avoiding the overlap and agglomeration of pure two-dimensional nanosheets. And the SEM images demonstrate that the final structure of numerous ordered CoNi-LDH "leaves" growing on the cross-linked CNT "branches" was achieved. TEM images of CoNi@NCNTs-LDH powders manually exfoliated from CC are shown in [Fig. 2e-g](#). It can be clearly observed that the outside of the carbon tube is surrounded by transparent folded nanosheets, and the boundary between the carbon tube (marked by the green line) and LDH (marked by the orange line)



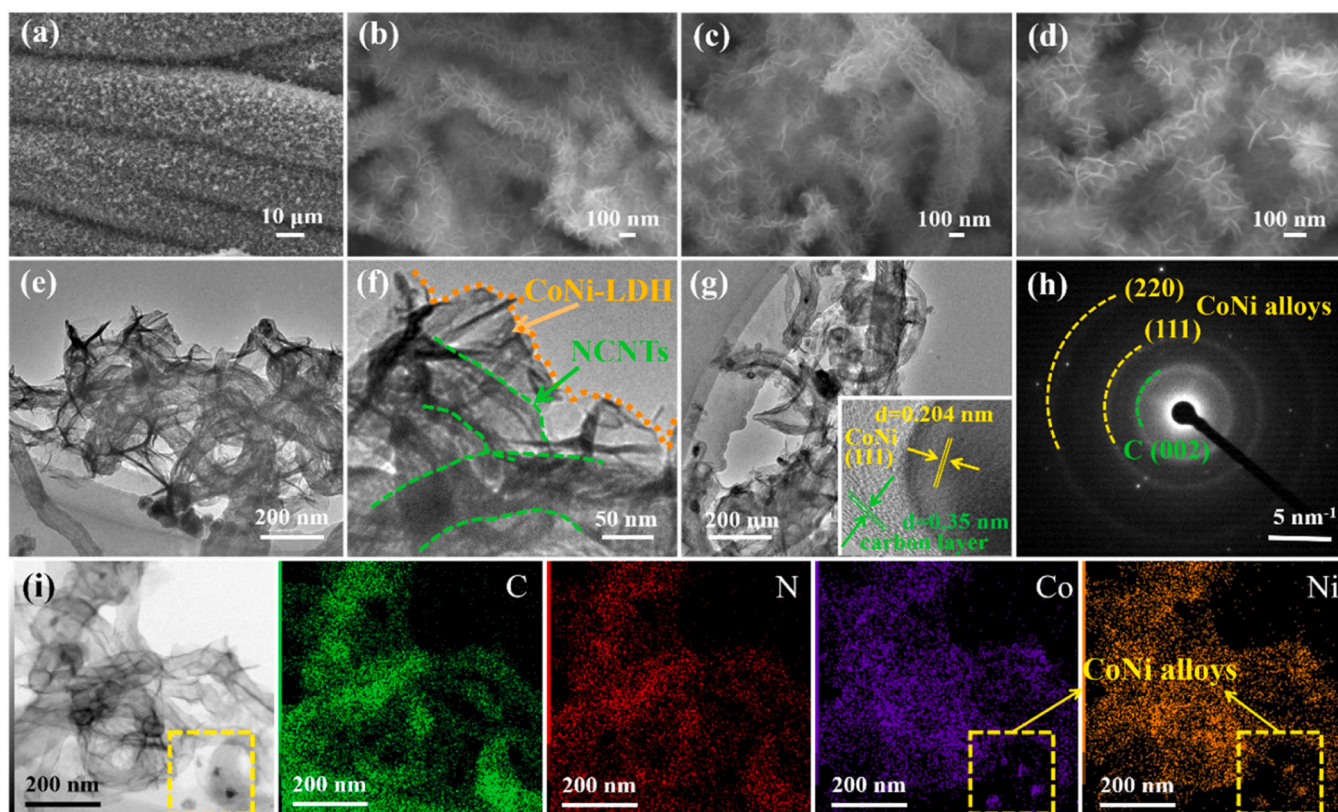


**Fig. 2.** (a-d) SEM images of CoNi@NCNTs-LDH/CC. (e-g) TEM images and (h) SAED pattern of CoNi@NCNTs-LDH powders. (i) Bright field STEM and corresponding EDS mapping images of CoNi@NCNTs-LDH powders.

can be detected. Meanwhile, the high-resolution TEM (Fig. 2g) and the selected area electron diffraction (SAED) pattern (Fig. 2h) both reveal the crystalline nature of CoNi alloy nanoparticles embedded with NCNTs, which is consistent with the XRD results. The bright-field scanning transmission electron microscopy (BF-STEM) image and energy dispersive X-ray analysis (EDX) mappings (Fig. 2i) indicate the heteroelemental distribution. Specifically, Co and Ni elements are highly uniformly distributed on nested particles, with the homogeneous dispersion of N and C in nanotubes, also demonstrating the structure of CoNi alloys embedded in N-doped carbon nanotubes. Additionally, it is observed that Co and Ni are concentrated on the outside of the carbon tube, which are strongly coincident with the LDH nanosheets, further confirming the "leaf-branch" composite structure of CoNi@NCNTs-LDH from another aspect.

Nitrogen adsorption-desorption analysis (Fig. S5a) displays a specific surface area of  $164 \text{ m}^2 \text{ g}^{-1}$  for CoNi@NCNTs-LDH, larger than that of CoNi@NCNTs ( $141 \text{ m}^2 \text{ g}^{-1}$ ), indicating that the leaf-branch structure after growing LDH nanosheets can effectively expose more surface area. And the pore size distribution curve (Fig. S5b) manifests the hierarchical porous structure of CoNi@NCNTs-LDH. The unique composite structure of the electrocatalyst can enable it additional structural advantages. The internal CoNi@NCNTs, as the branches, provide electron transport channels and play a remarkable supporting role. The external CoNi-LDH nanosheets, as the leaves, vertically distributed along the radial direction, will expose abundant specific surface areas. Thus desirable "leaf-branch" composite structure with open and ordered nanoarrays would greatly promote the contact between the reactants and the catalysts, which is conducive to the electrocatalytic reaction.

The property of CoNi@NCNTs-LDH composites prepared under different electrodeposition times were also explored. Fig. S6 shows the SEM images of the CoNi@NCNTs-LDH-100 samples under the electrodeposition treatment of 100 s, where the surface of nanotube is not entirely covered by CoNi-LDH under low mass loading, which exhibits a

lower specific surface area ( $153 \text{ m}^2 \text{ g}^{-1}$ , Fig. S7) than CoNi@NCNTs-LDH-300. When the electrodeposition time increases to 500 s, the increase of LDH nanosheets promotes a larger specific surface area ( $190 \text{ m}^2 \text{ g}^{-1}$ , Fig. S7). However, due to the excessive mass loading, the LDH layers overgrow and adhere to each other, resulting in partial overlapping coverage (Fig. S8). In addition, the pure CoNi-LDH/CC catalyst was also synthesized by direct electrodeposition on CC (Fig. S9), as a contrast sample. The carbon fibers are directly covered by vertically grown dense arrays of nanosheets via a facile in-situ growth method.

X-ray photoelectron spectroscopy (XPS) was employed to clarify the surface chemical compositions. The full spectrum identifies the co-existence of C, N, O, Co and Ni elements for CoNi@NCNTs-LDH/CC (Fig. S10), and after the growth of LDHs, there is a significant increase of the content of O, Co and Ni elements. The C1s spectra of CoNi@NCNTs-LDH/CC are mainly composed of C=C-C (284.8 eV), C=N (285.2 eV), and C-N/ C-O (286.2 eV) (Fig. S11a) [29–31]. N 1s XPS spectra include five peaks of pyridinic-N (398.7 eV), Co/Ni-N<sub>x</sub> (399.6 eV), pyrrolic-N (400.3 eV), graphitic-N (401.2 eV) and oxidized-N (402.8 eV) (Fig. S11b) [15,32,33]. Fitting the O 1s XPS spectra gives three peaks (Fig. S11c), belonging to Co/Ni-O (531.4 eV), OH<sup>-</sup> species (532.1 eV) and adsorbed oxygen species (533.3 eV) [29,34,35], where the combination with CoNi-LDH results in a high content of Co/Ni-O species. As for the high-resolution Co 2p and Ni 2p spectra (Fig. S11, S12), there are both obvious double main peaks along with two satellite peaks. The fitting peaks at 780.6 and 781.8 eV in Co 2p correspond to Co<sup>0</sup> metallic state and the Co<sup>2+</sup> oxidation state of Co 2p<sub>3/2</sub> peak [36,37]. Similarly, the fitting peaks of Ni 2p at 780.6 and 781.8 eV are inscribed to Ni<sup>0</sup> and Ni<sup>2+</sup> species [15]. And the Co<sup>0</sup> and Ni<sup>0</sup> peaks in Co 2p and Ni 2p spectra further manifest the existence of CoNi alloys in CoNi@NCNTs-LDH/CC.



### 3.2. Electrochemical performance

#### 3.2.1. Electrocatalytic ORR performance

The bifunctional electrochemical property of obtained self-supported CoNi@NCNTs-LDH/CC catalysts were evaluated in a typical three-electrode system. The ORR electrochemical measurements were firstly executed in oxygen-saturated 0.1 M KOH electrolyte with noble metal Pt/C as benchmark. As for CoNi@NCNTs-LDH/CC obtained under different electrodeposition time (Fig. S14), CoNi@NCNTs-LDH/CC-300 exhibits superior ORR activity, with a more positive ORR peak and higher onset potential ( $E_{\text{onset}}$ ) than that of CoNi@NCNTs-LDH/CC-100 and CoNi@NCNTs-LDH/CC-500, which may be due to the advanced “leaf-branch” nanostructure composed of CoNi@NCNTs and CoNi-LDH with relatively large specific surface areas. Thus, the CoNi@NCNTs-LDH/CC discussed below refers to the catalyst under the electrodeposition treatment of 300 s, unless otherwise specified.

The ORR performance of CoNi@NCNTs-LDH/CC and contrast samples were evaluated. Fig. 3a shows LSV curves of self-supported catalysts, which directly serve as the working electrode. The CoNi@NCNTs-LDH/CC displays higher current density and more positive  $E_{\text{onset}}$  and half wave potential ( $E_{1/2}$ ) than those of CoNi@NCNTs/CC, which is far higher than those of CoNi-LDH/CC, demonstrating the target catalyst displays better ORR catalytic activity. To evaluate catalyst performance clearly and intuitively, the powder catalysts were further measured by corresponding RDE and RRDE tests, stripped from the self-supported catalysts. From Fig. 3b, the CoNi@NCNTs-LDH powders display the  $E_{1/2}$  of 0.84 V, more positive than that of CoNi@NCNTs contrast samples (0.81 V), which is even superior to that of Pt/C benchmark (0.82 V), and other reported transition metal-based electrocatalysts (Table S1), manifesting the considerable ORR catalytic property. As exhibited in Fig. 3c, CoNi@NCNTs-LDH has an obviously smaller Tafel slope value (77 mV  $\text{dec}^{-1}$ ), in comparison with that of the reference samples of

CoNi@NCNTs (81 mV  $\text{dec}^{-1}$ ) and Pt/C catalysts (128 mV  $\text{dec}^{-1}$ ), also demonstrating the effectively accelerated ORR kinetics of CoNi@NCNTs-LDH. To investigate the reaction mechanism, LSV curves of CoNi@NCNTs-LDH obtained at different rotation speeds (400–2025 rpm) are recorded in Fig. 3d, and corresponding Koutecky-Levich (K-L) plots are displayed in the insert. It shows that there is a perfect linear relationship under different potentials (0.3–0.5 V), indicating the first-order reaction kinetics of dissolved oxygen concentration. The electron transfer number ( $n$ ) of CoNi@NCNTs-LDH based on K-L plots is calculated to be 3.89–3.91, suggesting that the CoNi@NCNTs-LDH catalyst complies with a highly efficient  $4e^-$  transfer process. Fig. 3e shows the  $\text{HO}_2$  yield and  $n$  derived from RRDE results, where the  $\text{HO}_2\%$  of CoNi@NCNTs-LDH is below 15 % at all potentials and its corresponding average  $n$  value is between 3.73 and 3.89. The low  $\text{HO}_2$  yields and high  $n$  values of CoNi@NCNTs-LDH are comparable to those of precious metal Pt/C catalysts, but obviously superior to those of CoNi@NCNTs contrast samples, which further manifests CoNi@NCNTs-LDH follows a four-electron-transfer process with high oxygen reduction efficiency. Beyond the ORR activity, the stability of CoNi@NCNTs-LDH were also investigated by chronoamperometric measurements (Fig. 3f). After constant operation under 0.7 V, CoNi@NCNTs-LDH can still retain 88.6 % of initial current density during operation for 16 h, while there is a current decrease up to 15 % of Pt/C catalysts during operation for 7 h, which verifies the enhanced stability of CoNi@NCNTs-LDH during electrocatalytic ORR process. Besides, after 1000 CV cycles, there is an inconspicuous difference in the half wave potential and diffusion current density in the LSV polarization curve from that of the initial one (Figure S15), manifesting the strong cycling durability of CoNi@NCNTs-LDH for ORR.

#### 3.2.2. Electrocatalytic UOR performance

The UOR electrocatalytic activity measurements of as-prepared self-

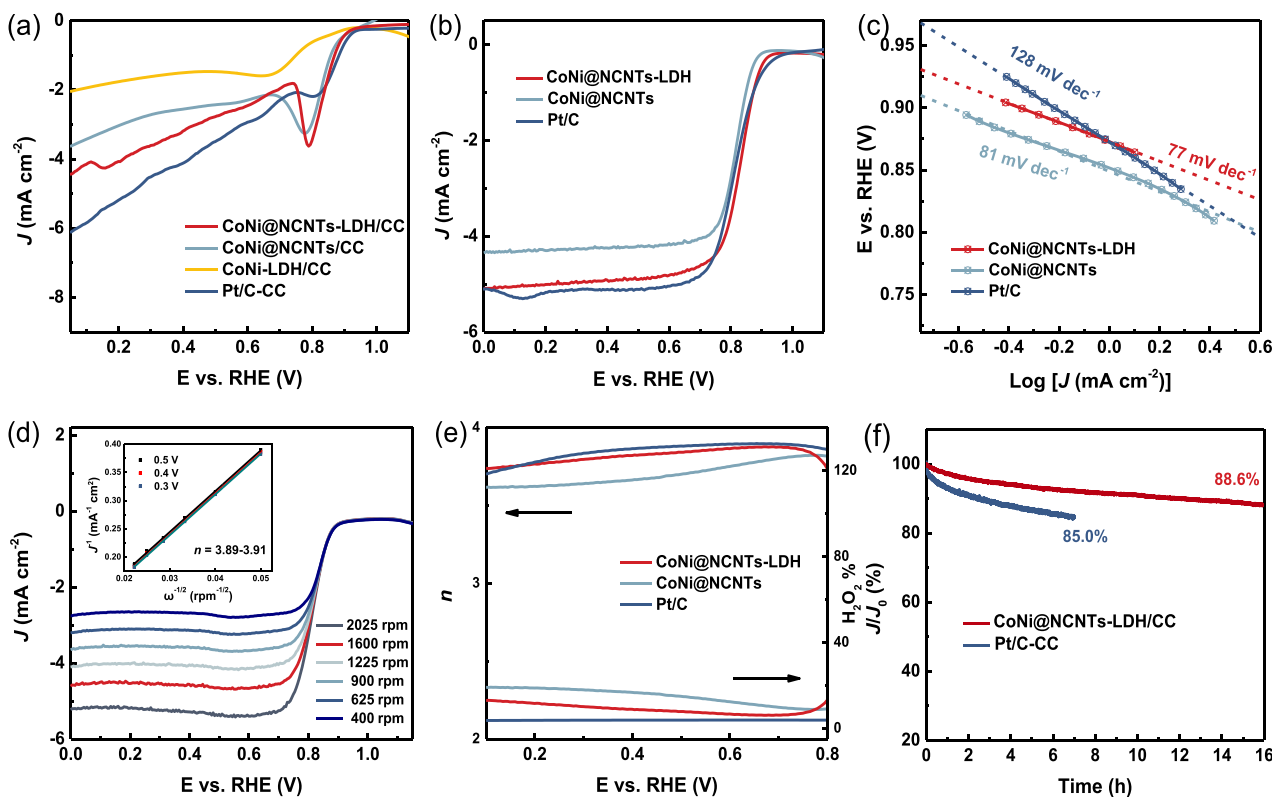


**Fig. 3.** ORR LSV curves of (a) prepared self-supported catalysts and (b) powder catalysts. (c) ORR Tafel plots of powder catalysts. (d) LSV curves under different rotating speeds for CoNi@NCNTs-LDH powders, and the inset is K-L plots at 0.5–0.3 V. (e)  $\text{HO}_2$  yield and  $n$  calculated by the RRDE measurements. (f) The chronoamperometric response for CoNi@NCNTs-LDH /CC and Pt/C-CC catalysts.



supported catalysts were then executed. In this work, considering that the human urine contains 2–2.5 wt% urea (approximate 0.33 M) [9], the concentration of urea in the electrolyte is selected as 0.33 M. Likewise, among CoNi@NCNTs-LDH/CC-x samples obtained through different electro-deposition treatment time (Fig. S16), the CoNi@NCNTs-LDH/CC-300 also exhibits the highest UOR activity with lowest overpotential. And the UOR performance of CoNi@NCNTs-LDH/CC discussed below refers to that obtained under the electrodeposition treatment of 300 s.

Fig. 4a displays UOR and OER LSV curves of CoNi@NCNTs-LDH/CC measured in 1.0 M KOH with 0.33 M urea and 1.0 M KOH, respectively. The current density of  $10 \text{ mA cm}^{-2}$  can be achieved at only 1.36 V ( $^{\text{UOR}}E_{j=10}$ ) for UOR process, which is obviously lower compared to OER potential (sharply decreased by 0.19 V). The effect of scan rate on the UOR property for CoNi@NCNTs-LDH/CC was investigated by performing CV measurements (Fig. 4b). The inset of Fig. 4b shows that the current density increases with increasing scan rates, consistent with the first-order power law relationship between the peak anodic current density and scan rate, indicating a mixed control of diffusion and capacitive behavior in the UOR [38,39]. As for the UOR performance of different contrast samples (Fig. 4c), CoNi-LDH/CC displays an obviously lower  $^{\text{UOR}}E_{j=10}$  (1.37 V) than that of CoNi@NCNTs/CC (1.44 V), implying the superior electrocatalytic UOR property of CoNi-LDH compared with CoNi@NCNTs. Furthermore, CoNi@NCNTs-LDH/CC shows the lowest overpotential value among the prepared samples at different current density (Fig. 4d), even superior to that of  $\text{RuO}_2/\text{CC}$  benchmark, indicating that the activity of CoNi@NCNTs-LDH catalyst is synergistically improved after the combination of the two components. Compared to the previously reported transition metal-based electrocatalysts, the CoNi@NCNTs-LDH/CC also exhibits comparatively

favorable UOR activity (Table S2).

To investigate the kinetics, Fig. 4e depicts the corresponding Tafel slopes of catalysts derived from the LSV curves. CoNi@NCNTs-LDH/CC displays a smallest Tafel slope of  $97 \text{ mV dec}^{-1}$ , in comparison with contrast samples of CoNi-LDH/CC ( $105 \text{ mV dec}^{-1}$ ) and CoNi@NCNTs/CC ( $159 \text{ mV dec}^{-1}$ ), as well as  $\text{RuO}_2/\text{CC}$  ( $124 \text{ mV dec}^{-1}$ ), demonstrating the accelerated UOR kinetics for CoNi@NCNTs-LDH/CC. The long-term UOR stability is evaluated by chronoamperometric measurements at the potential of 1.36 V (Fig. 4f), where unobvious change of current density can be observed after constant operation for 20 h. Additionally, after 1000 cycles, there is no significant difference in anode current density compared with the initial one, thus manifesting the robust durability of CoNi@NCNTs-LDH/CC for electrocatalytic UOR process.

### 3.2.3. Reaction mechanisms of CoNi@NCNTs-LDH/CC

Considering the excellent properties of the CoNi@NCNTs-LDH/CC electrocatalyst, in-depth exploration on the origin of its high bifunctional activity is expected to reveal new insights for the structure-performance relationship and provide guidance for further rational design of bifunctional electrocatalysts. From the above electrocatalytic results, the contrast sample of CoNi@NCNTs/CC exhibits superior ORR activity than CoNi-LDH/CC sample, but the UOR property of CoNi-LDH/CC is better than that of CoNi@NCNTs/CC instead, which suggests that CoNi@NCNTs/CC and CoNi-LDH/CC are more efficient for ORR and UOR process, respectively. In addition, the ORR and UOR activity of the CoNi@NCNTs-LDH/CC electrocatalyst exceeds the corresponding pure components (CoNi@NCNTs/CC and CoNi-LDH/CC), which indicates an inherent synergy between two components, leading to further enhancement of ORR and UOR bifunctional activity. Then, the origin of the enhanced synergistic activity and the active sites were explored, for

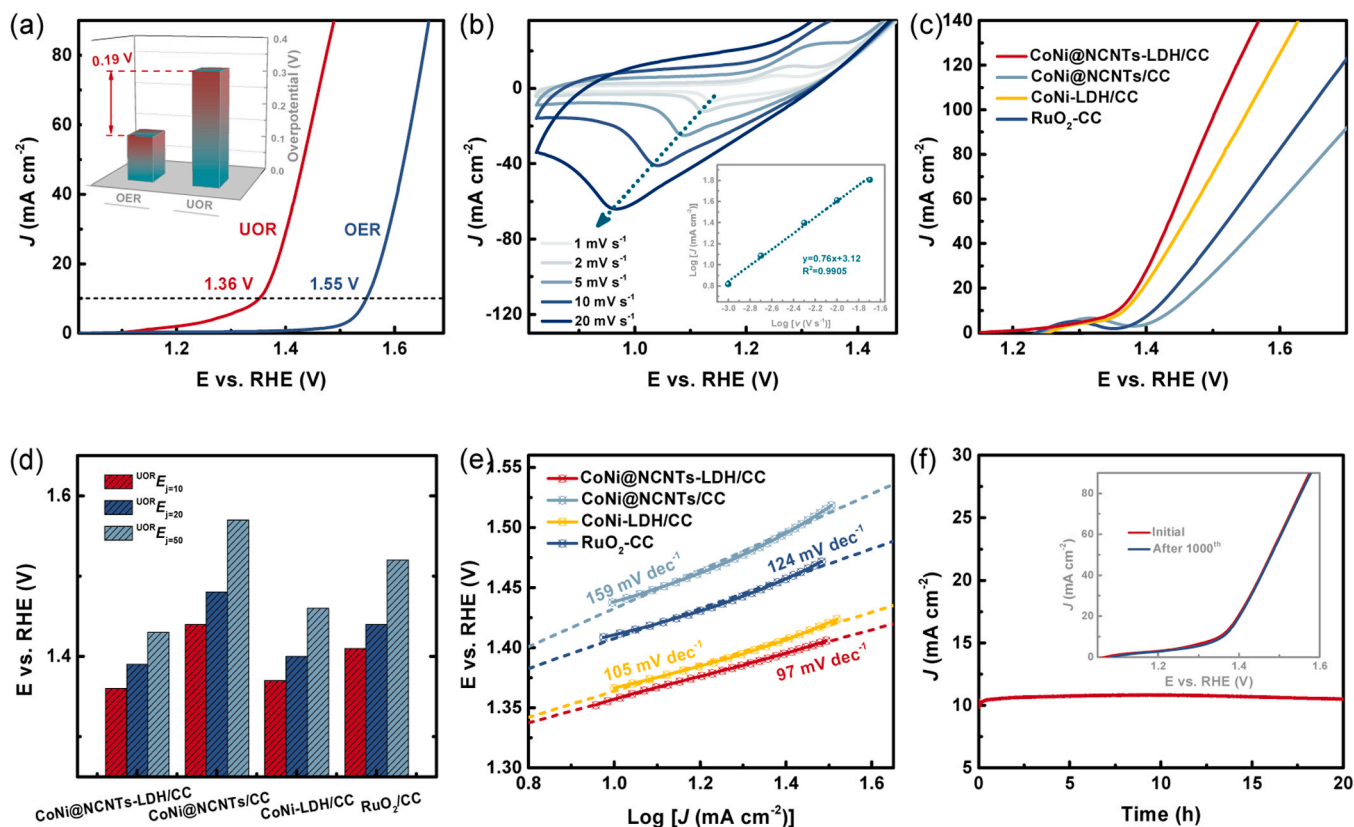
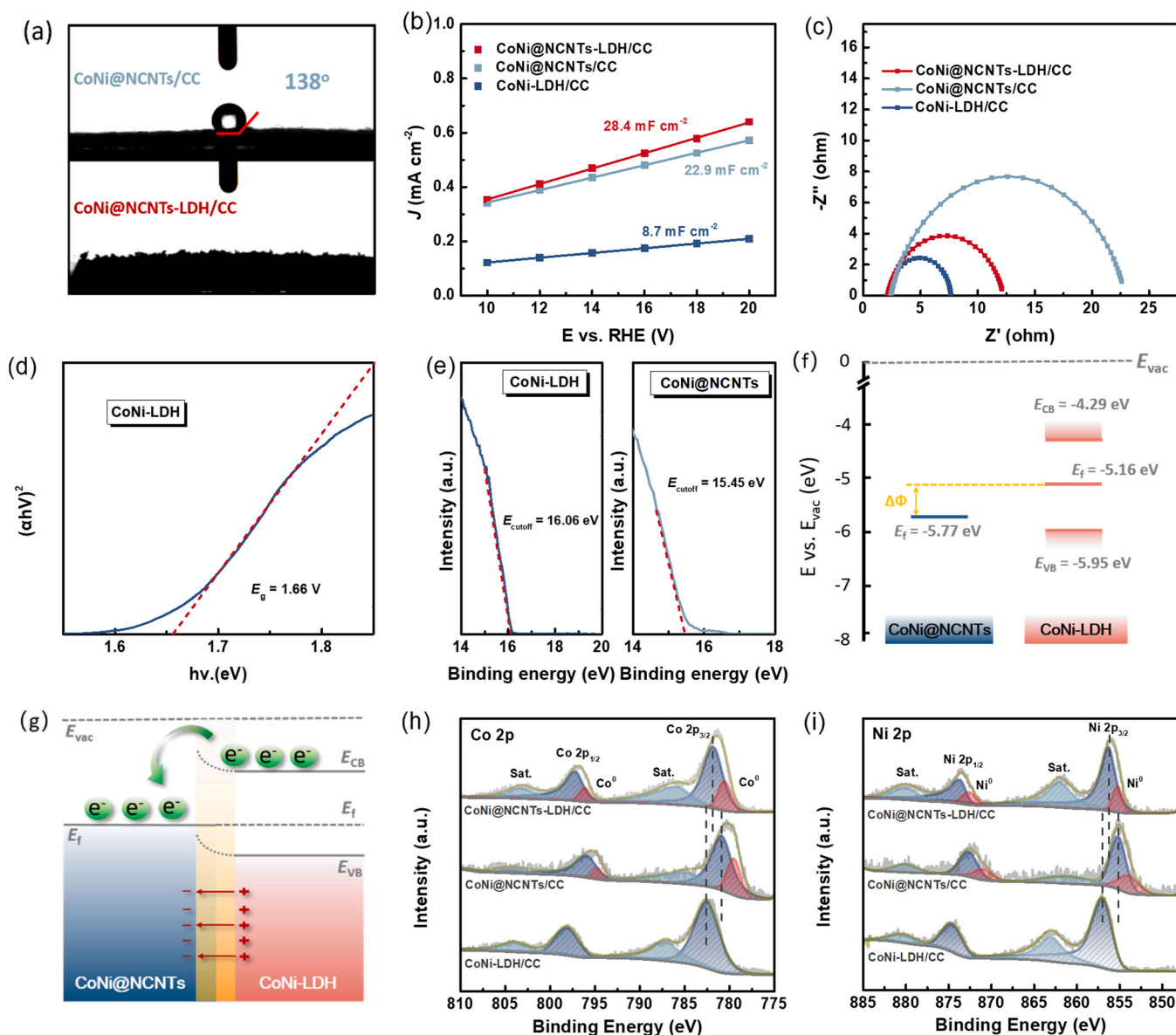


Fig. 4. (a) LSV curves of CoNi@NCNTs-LDH/CC for UOR and OER. (b) Cyclic voltammograms of CoNi@NCNTs-LDH/CC at different scan rates. The inset is the plot of the logarithm of cathodic peak current density against the logarithm of scan rates. (c) LSV curves of different catalysts for UOR in 1.0 M KOH + 0.33 M urea. (d) The comparison of UOR potential of different catalysts. (e) Tafel slopes of different catalysts for UOR process. (f) The chronoamperometric responses of CoNi@NCNTs-LDH/CC, and the inset is the polarization curve before and after 1000 CV cycles.



further investigation of the bifunctional reaction mechanism based on our target catalysts. Firstly, the biomimetic CoNi@NCNTs-LDH/CC catalyst exhibits a “leaf-branch” shape structure, where the CoNi@NCNTs components serve as the branch with the CoNi-LDH as the leaf. In nature, this structure has unique advantages. On the one hand, the luxuriant leaves grow sequentially directly onto the branches in order, exposing large areas of the leaves to better utilize light for photosynthesis, thus creating nutrient supplies to the whole body. On the other hand, the branches not only serve as the supports to keep the leaves stable in strong winds, but also provide constant nutrition for the growth of leaves. The branches and leaves are complementary, interdependent and mutually reinforcing, forming an organic whole. In this regard, the effect of the unique leaf-shaped structure of CoNi@NCNTs-LDH/CC catalyst on electrocatalytic ORR and UOR is investigated. As is shown in Fig. 5a, CoNi@NCNTs has a high hydrophobicity with a contact angle of  $138^\circ$ , reducing the accessibility of the electrolyte in ORR process. CoNi-LDH is hydrophilic, and the composition with LDH significantly improves the hydrophilicity of the composite, which

exhibits hydrophilic property. In addition, the electrochemically active surface area ( $C_{dl}$ ) was obtained by executing CV tests with different scan speeds (10, 12, 14, 16, 18, and 20  $\text{mV s}^{-1}$ ), to evaluate the exposed electrochemically active surface area (ECSA) (Fig. S17). By calculating the slope of plots of current density versus the scan rate, the  $C_{dl}$  of CoNi@NCNTs-LDH/CC is determined to be  $28.4 \text{ mF cm}^{-2}$ , higher than that of CoNi@NCNTs/CC ( $22.9 \text{ mF cm}^{-2}$ ) and CoNi-LDH/CC ( $8.7 \text{ mF cm}^{-2}$ ) (Fig. 5b). The results indicate that the ECSA of the composite materials is higher than that of single-component catalysts. Growing a large number of LDH nanosheet (leaves) on the carbon nanotubes (branches) increases the ECSA of the composite catalyst, which distinctly promotes the exposure of active surface area with accessible active sites and the sufficient contact between active sites and electrolyte, thus enabling the CoNi@NCNTs-LDH/CC composites enhanced ORR electrocatalytic performance than the single-component catalysts. While, as for UOR process, CoNi-LDH displays a higher intrinsic activity, but the inherent property of poor conductivity limits the performance of electrocatalytic reaction. In this respect, the CoNi@NCNTs carbon



**Fig. 5.** (a) The contact angle of CoNi@NCNTs/CC and CoNi@NCNTs-LDH/CC. (b)  $C_{dl}$  obtained from CV curves at different scan rates. (c) Nyquist plots of different catalysts. (d) UV-vis spectra of CoNi-LDH/CC. (e) UPS spectra of CoNi-LDH/CC and CoNi@NCNTs/CC. (f) Energy-band alignment diagram. (g) Schematic illustration of the Mott-Schottky junction. (h) Co 2p and (i) Ni 2p XPS spectra for catalyst powders.



material has excellent electrical conductivity (Fig. 5c), and the combination with CoNi@NCNTs greatly reduces the charge transfer resistance, and facilitates the electron transport capacity, enabling the CoNi@NCNTs-LDH with enhanced UOR performance. To sum up, the "leaf-branch" composite catalyst composed of electrically conductive CoNi@NCNTs and hydrophilic CoNi-LDH exhibits a structural advantage similar to "leaf-branch coordination". The "leaf" (CoNi-LDH) and "branch" (CoNi@NCNTs) complement each other's advantages in structure. The combination of the two parts not only improves the hydrophilicity of the composite, promotes the contact between the reactants and active sites, but also strengthens the ion and electron pathway. Thus, they jointly promote the synergistic effect of the composite CoNi@NCNTs-LDH/CC electrocatalyst to further provide the remarkable bifunctional properties.

For plants in nature, luxuriant leaves are the place for photosynthesis and the main sites for nutrient production, while the continuous growth of plants depends on the supply through branches, which are considered to be the main site of nutrient reserves. The exchange of materials between two sites is essential for the realization of both functions. It is noteworthy that there is a directional transfer of substances between two organs of leaves and branches, that is, thanks to the selective permeation of the cell membranes at the leaf-branch interface, the organic substances can be transmitted from leaves to branches, and then transported to the whole body, while inorganic substances are continuously transported from branches to leaves. Thus, it is the mechanism of the exchange of substances which unites the two organs and promotes the fulfillment of both the functions of plants. Inspired by the contribution of interfacial material exchange mechanisms to the dual functions for plants, for the CoNi@NCNTs-LDH/CC composite catalysts, the internal interaction between CoNi@NCNTs (leaves) and LDH (branches) active components and the contribution to the bifunctional activity for CoNi@NCNTs-LDH/CC were further explored. It has been reported that the combination of different components can change the electron densities of atoms around the interfaces, which would affect the absorption of the target ions and charge transfer during electrocatalysis. In order to deeply understand the information of charge redistribution, and explore the essence of synergy and interaction between CoNi@NCNTs and LDH, the Mott-Schottky (M-S) and ultraviolet-visible spectroscopy (UV-vis), ultraviolet photoelectron spectroscopy (UPS) measurements were executed to obtain the energy diagram. From the M-S plots (Fig. S18), CoNi-LDH displays a positive slope, representing the *n*-type semiconductor property with the flat band potential ( $E_{FB}$ ) of  $-0.21$  V (vs. RHE,  $-4.29$  eV vs. vacuum level) [40]. There is a difference of  $0.2$  V between the conduction band (CB) potential ( $E_{CB}$ ) of *n*-type semiconductor and the  $E_{FB}$ , and thus the  $E_{CB}$  of CoNi-LDH can be calculated to be  $-4.09$  eV. Then, the band gap energies ( $E_g$ ) are obtained by UV-vis measurements, as shown in Fig. 5d. From the Tauc plots of  $(ah\nu)^2$  against the photon energy, the  $E_g$  value of CoNi-LDH is estimated to be  $1.66$  eV [41]. The UPS measurements were carried out to investigate the surface electronic property of CoNi-LDH and CoNi@NCNTs (Fig. S19 and Fig. 5e). The work function ( $\Phi$ ) is calculated to be  $5.16$  and  $5.77$  eV for CoNi-LDH and CoNi@NCNTs, respectively. The difference in  $\Phi$  between CoNi-LDH and CoNi@NCNTs builds a Mott-Schottky junction (Fig. 5f), and the  $\Delta\Phi$  will drive the charge flow from high level to low until the system reaches an equilibrium [41,42]. Upon intimate contact, the electrons in CoNi-LDH flow into CoNi@NCNTs until the  $E_f$  turns to be aligned, leaving the positively ionized donor behind. Accordingly, a built-in electric field is constructed with the direction from CoNi-LDH to CoNi@NCNTs, which results in opposite space-charge region at the interface of CoNi@NCNTs/LDH and further leads to energy level shifting and band edge bending (Fig. 5g). In addition, XPS spectra can also confirm this conclusion. For the Co 2p core-level spectra (Fig. 5h), CoNi@NCNTs-LDH/CC shows the characteristic peaks of Co  $2p_{3/2}$  and  $2p_{1/2}$  at  $781.8$  and  $779.3$  eV, respectively, which displays a significantly positively shifted binding energy compared with CoNi@NCNTs/CC ( $780.9$  eV for Co  $2p_{3/2}$  and  $796.0$  eV for Co  $2p_{1/2}$ ), but a negatively

shifted one compared with CoNi-LDH/CC ( $782.5$  eV for Co  $2p_{3/2}$  and  $798.1$  eV for Co  $2p_{1/2}$ ). Similarly, in the Ni 2p region (Fig. 5i), the Ni  $2p_{3/2}$  and  $2p_{1/2}$  peaks for CoNi@NCNTs-LDH/CC composites exhibit obvious positive shifts in comparison with CoNi@NCNTs/CC, with negative shifts compared with CoNi-LDH/CC. The shifts in BEs reflect diverse changes of electronic structures, which also verifies the formation of internal electric field for CoNi@NCNTs-LDH/CC composites. After forming a Mott-Schottky junction, electrons are transferred from CoNi-LDH, *n*-type semiconductors, to CoNi@NCNTs, which tends to act as electron-acceptor sites, leading to a negative shift of the BE of CoNi@NCNTs-LDH compared with pure CoNi-LDH [41,43]. As a consequence, a more efficient and stronger positive charge active center can be established at CoNi-LDH surface, which is conducive to accelerating the transfer of electrons derived from  $OH^-$  to valence band (VB) of CoNi-LDH, followed by the subsequent recombination between the holes at VB of CoNi-LDH and the electrons from  $OH^-$  [40]. And the redundant electrons on the CB of CoNi-LDH are then diverted to CoNi@NCNTs to restore and maintain the charge balance. Thus the surface of CoNi-LDH is conducive to the adsorption of  $OH^-$ , which contributes to the efficient UOR catalysis on CoNi-LDH surface. On the contrary, as for ORR electrolysis process, due to the built-in electric field with the direction from CoNi-LDH to CoNi@NCNTs, the surface of CoNi@NCNTs is expected to be favorable for the adsorption of proton intermediates, thus promoting the ORR electrocatalytic reaction.

To further explore the effect of the built-in electric field on the electron structure at the interface, the density functional theory (DFT) calculations were executed to investigate the electron migration and further reveal the reaction mechanism. As shown in Fig. 6a, the optimized CoNi@NCNTs-LDH interface structure models was constructed. The charge density difference at the interface is calculated, as shown in Fig. 6b. It can be observed that the additional charge is skewed around the LDH site and about  $1.7$  e flows from LDH to CoNi@NCNTs due to the strong built-in electric field. Thus, the electronic analysis demonstrates a correlated interaction between LDH and CoNi@NCNTs, consistent with previous results. Fig. 6c depicts the density of states (DOS) of the catalysts. According to the d-band center theory, the ideal binding energy should be neither strong nor weak, and the binding energy between adsorbent and adsorbent is closely related to the highly localized metal d state [41,44]. Among prepared catalysts, CoNi@NCNTs-LDH composite has a d band center of  $-1.27$  eV, manifesting moderate binding energies, compared to CoNi@NCNTs ( $-1.12$  eV) and LDH ( $-1.54$  eV), which suggests a mild adsorption/desorption process and a more favorable electrochemical process.

The Gibbs free energy for each elementary step in ORR and UOR process has been calculated to further unravel the mechanism for the superior catalytic activities of CoNi@NCNTs-LDH composite. As for CoNi@NCNTs-LDH, considering the charge imbalance due to the built-in electric field from CoNi-LDH to CoNi@NCNTs, the Gibbs free energy at LDH sites and CoNi sites are respectively calculated. During ORR process, firstly, the adsorption properties of  $O_2$  are compared, and there is a higher adsorption energy at CoNi sites ( $0.76$  eV) of CoNi@NCNTs-LDH, compared with CoNi@NCNTs samples ( $0.55$  eV). It indicates that  $O_2$  has a stronger trend to be adsorbed on the surface of CoNi side in the CoNi@NCNTs-LDH compared to individual CoNi@NCNTs due to the presence of the built-in electric field [45]. As shown in Fig. 6d, for the CoNi sites of CoNi@NCNTs-LDH composite and CoNi@NCNTs catalysts, the  $OOH^*$  intermediates formation step is the rate-determining step (RDS), and the transformation of  $OOH^*$  to  $O^*$  is the RDS for LDH sites of CoNi@NCNTs-LDH composite and CoNi-LDH catalysts. Compared with the contrast sample of CoNi@NCNTs and CoNi-LDH, there is the lowest thermodynamic barrier of  $0.90$  eV, which reveals that CoNi@NCNTs-LDH is more favorable for the subsequent ORR steps, and a lower overpotential of CoNi@NCNTs-LDH further confirmed the favorable kinetics [46,47]. This suggests that due to the presence of an electron-rich center on the CoNi@NCNTs surface, derived from the internal electric field from CoNi-LDH to CoNi@NCNTs, the CoNi sites



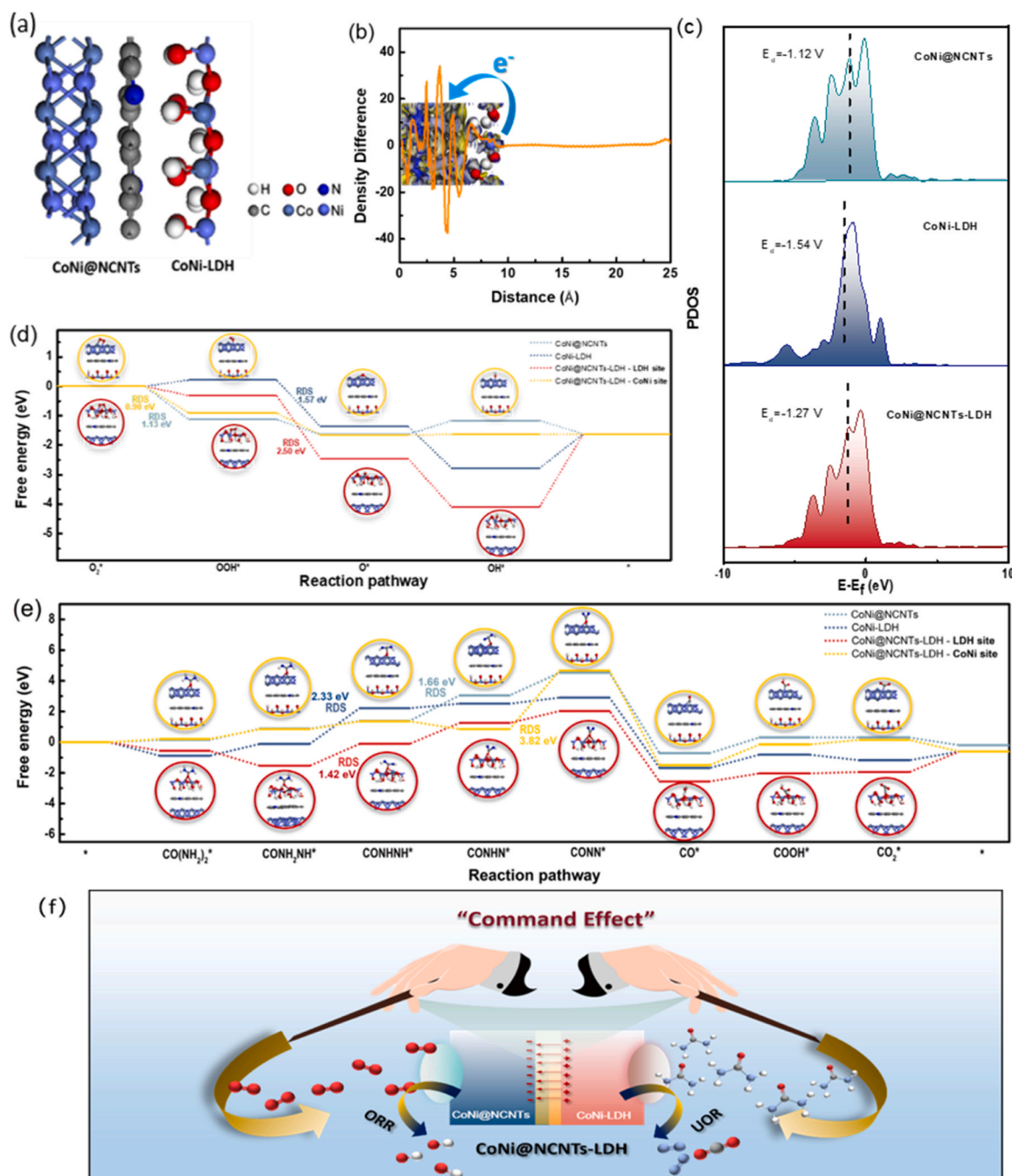


**Fig. 6.** (a) Side view of atomic structure models of CoNi@NCNTs-LDH interface. (b) Calculated charge density distribution at the CoNi@NCNTs-LDH interface, and blue and yellow refer to electron-rich and electron-deficient areas, respectively. (c) Comparison of DOS of the d-band for CoNi@NCNTs, CoNi-LDH and CoNi@NCNTs-LDH. Gibbs free energy diagram for (d) ORR and (e) UOR process on CoNi@NCNTs, CoNi-LDH and CoNi@NCNTs-LDH composite. (f) Schematic illustration of "command effect" for CoNi@NCNTs-LDH/CC.

would promote the adsorption of O<sub>2</sub>. At the same time, the CoNi sites with lower thermodynamic energy barriers are conducive to the conversion of intermediates (O<sup>\*</sup>, OH<sup>\*</sup>) and thus promotes the subsequent ORR reaction steps, which are demonstrated as the main reaction sites for ORR process. As for UOR process, in order to understand the inherent reactivity of the electrochemical oxidation of urea on the catalyst surface, it is proposed that urea dissociation consists of four steps, namely urea adsorption, dehydrogenation, N-N coupling and CO<sub>2</sub> desorption [48,49]. As shown in Fig. 6e, the urea molecule adsorption is thermodynamically favorable on the LDH sites of CoNi@NCNTs-LDH and CoNi-LDH. And there is stronger adsorption at LDH sites (0.89 eV) of CoNi@NCNTs-LDH than CoNi-LDH sample (0.56 eV), which means that

urea molecules are easily adsorbed at the LDH sites of CoNi@NCNTs-LDH sample. Then the adsorbed urea molecule is first oxidized and dehydrogenated to form \*NHCONH<sub>2</sub> via proton-coupled electron transfer. The \*NHCONH<sub>2</sub> can be further oxidized into \*NHCONH, \*CONN, and \*CO through oxidative dehydrogenation [48, 49]. For the LDH sites in CoNi@NCNTs-LDH sample and CoNi-LDH sample, the dehydrogenation process from \*NHCONH<sub>2</sub> to \*NHCONH is the RDS, while the transformation from \*NHCONH to \*NCONH and from \*NCONH to \*CONN are the thermodynamically limiting steps for CoNi@NCNTs sample and CoNi sites in CoNi@NCNTs-LDH sample, respectively. By comparison, it can be obviously found that the LDH sites in CoNi@NCNTs-LDH complex possesses the lowest thermodynamic



barrier in RDS (1.42 eV) of the UOR process. Combining experimental data and theoretical calculation, it precisely suggests that, owing to the existence of the built-in electric field, the surface of LDH sites in CoNi@NCNTs-LDH composite provide electron-deficient centers, which strengthens the adsorption of urea molecules and OH<sup>-</sup> reactants, further greatly promotes the dehydrogenation steps in UOR process, thus enabling the LDH sites with strong activity towards UOR [50]. Therefore, for the leaf-branch shaped CoNi@NCNTs-LDH/CC catalysts, the internal electric field is formed at the interface after the composite of CoNi@NCNTs (leaves) and LDHs (branches), which changes the electron densities of atoms around the interface, forming positively charged active centers on the LDH surface and negatively charged active centers on the CoNi@NCNT surface. In this way, a "command effect" (Fig. 6f) is formed during the UOR and ORR electrocatalysis process, which induces the directional movement of the respective reactants to the active component surface of catalysts, and effectively triggers the interfacial accumulation of reactants around the different sites. Accordingly, a two-site catalyst is constituted of CoNi@NCNTs-LDH/CC, in which the O<sub>2</sub> reactants move directionally to the highly active CoNi sites in ORR reaction, while for UOR reactions, the urea molecular reactants aggregate at the LDH sites, where the UOR reaction mainly occurs, thus resulting in the efficient catalytic activity of CoNi@NCNTs-LDH/CC for both ORR and UOR.

To sum up, inspired by the photosynthesis of green plants in nature based on the cooperation of branches and leaves, a binary-site catalyst design of CoNi@NCNTs-LDH is developed for specific ORR-UOR electrocatalytic process (Fig. 7). On the one hand, the leaf-branch-shaped catalysts exhibit ingenious structural advantages. The CoNi@NCNTs branches and CoNi-LDH leaves are spatially separated, serving as the main sites for ORR and UOR reactions, respectively, with each of them performing its own function. At the same time, the structural advantages complement each other to make up for the deficiency of a single component, which comprehensively improves the hydrophilicity of the composites and strengthens the ionic and electronic pathways, providing suitable reaction microenvironments for their respective reactions and promoting the efficient performance of ORR and UOR for CoNi@NCNTs-LDH/CC catalysts. On the other hand, between the two components of CoNi@NCNTs branches and CoNi-LDH leaves, there is a material exchange mechanism similar to that between the branches and leaves of green plant. For CoNi@NCNTs-LDH/CC catalysts, an internal electric field from CoNi@NCNTs to CoNi-LDH, with electrons flowing from CoNi-LDH to CoNi@NCNTs, forming positively charged active centers on the surface of CoNi-LDH and negatively charged active centers on the surface of CoNi@NCNTs. The charged surfaces would have great effect on the absorption of targeted ions and charge-transfer process during catalysis. Under the induction of the "command effect", the reaction intermediates of ORR and UOR are directed to the surfaces of CoNi@NCNTs and CoNi-LDH active centers, respectively, which lead to the aggregation of the substrates for ORR and UOR, and promote the

efficient electrocatalytic reactions in the respective reaction sites.

### 3.3. Metal-air battery measurements

A conventional rechargeable ZAB was firstly constructed with CoNi@NCNTs-LDH/CC directly as the air cathode. From Fig. 8a, assembled ZAB can hold a high open-circuit voltage (OCV) of 1.496 V. The peak power density of the ZAB assembled with CoNi@NCNTs-LDH/CC reaches up to 153 mW cm<sup>-2</sup> at 242 mA cm<sup>-2</sup>, higher than that of Pt/C-IrO<sub>2</sub> based ZAB (Fig. 8b). Besides, as clarified by the charging-discharging polarization curves (Fig. 8c), CoNi@NCNTs-LDH/CC-based ZAB obviously exhibits a lower charging-discharging voltage gap than that based on Pt/C-IrO<sub>2</sub> catalysts. The above results manifest that, profited by the effective bifunctional property of prepared CoNi@NCNTs-LDH/CC catalysts, the constructed ZAB has exhibited superior charging-discharging property than that based on precious Pt/C-IrO<sub>2</sub> catalysts.

In order to further improve the performance for the charging process, thus reducing the charging and discharging voltage gap and achieving high energy efficiency, a urea-assisted rechargeable ZAB was constructed by coupling ORR and UOR in the electrolyte of 6 M KOH + 0.33 M urea with the CoNi@NCNTs-LDH/CC as the air cathode, according to the model diagram (Fig. 1a). As shown in Fig. S20, the assembled urea-assisted ZAB can deliver an OCV of 1.489 V, which is close to that of the conventional ZAB (Fig. 8a). Fig. 8d shows the discharging polarization curves and the corresponding power density curves, where the urea-assisted ZAB exhibits a peak power density of 148 mW cm<sup>-2</sup> at 232 mA cm<sup>-2</sup>, which is only slightly lower than that of conventional ZAB, revealing a negligible influence of urea introduction on the discharge power density of ZAB. However, from the charging-discharging polarization curves (Fig. 8e), the urea-assisted ZAB shows a significantly lower charging voltage compared with that of conventional ZAB, implying the influence of urea introduction on the charging process of ZABs. There is a lower charging-discharging potential gap than that of conventional ZAB at different current densities, revealing a more efficient recharge property of improved urea-assisted ZAB. Then, the galvanostatic charging measurements of urea-assisted ZABs at different current densities were executed to further explore the improvement of the charging process (Fig. 8f). Distinctly, the charging voltage of urea-assisted ZAB under the current densities from 1 to 20 mA cm<sup>-2</sup> is lower than that of conventional ZAB, contributing to 7 %–10 % energy conservation during the charging process. This illustrates that the substitution of OER with UOR (coupling UOR and ORR) in the air electrode of ZAB can effectively reduce the charging voltage and thus improving the overall energy conversion efficiency. In addition, the urea degradation can be achieved simultaneously during the charging process of urea-assisted ZAB, and the capability of urea elimination in the actual operation of the constructed ZAB device is also evaluated. The urea elimination rates were measured using the urease method after

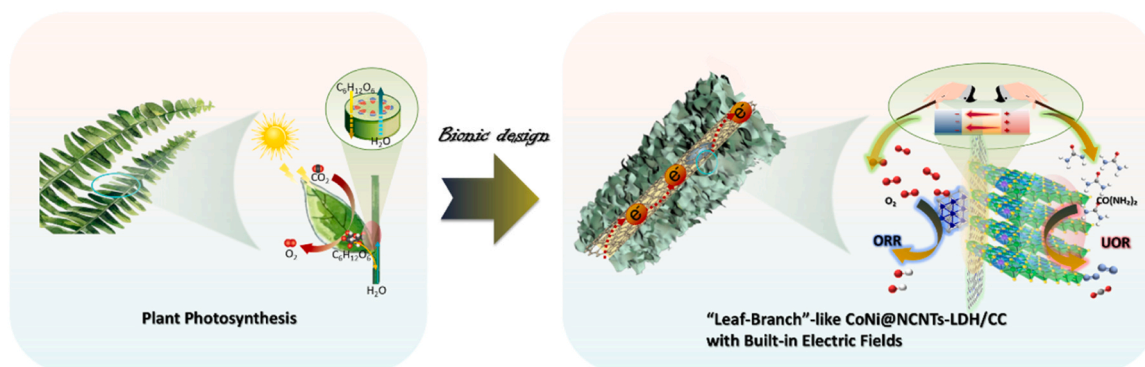
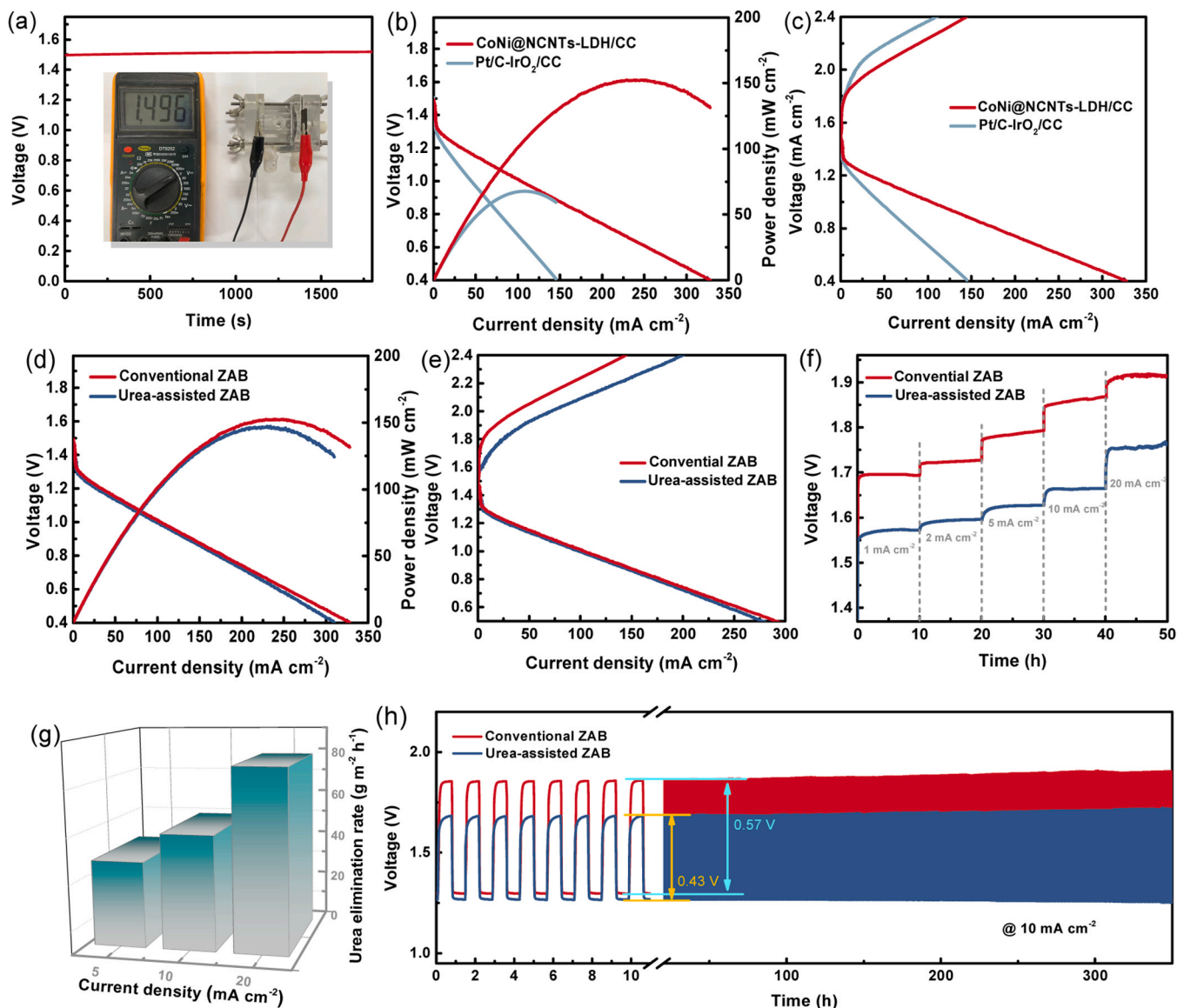


Fig. 7. Reaction mechanisms of binary-site catalyst of leaf-branch-shaped CoNi@NCNTs-LDH.





**Fig. 8.** (a) Open circuit plot of a ZAB based on CoNi@NCNTs-LDH/CC. (b) Charge-discharge curves and the power density curves of CoNi@NCNTs-LDH/CC and Pt/C-IrO<sub>2</sub>/CC based ZABs (c) Charging/discharging polarization curves of CoNi@NCNTs-LDH/CC and Pt/C-IrO<sub>2</sub>/CC based ZABs. (d) Charge-discharge curves and the power density curves for conventional and urea-assisted ZABs. (e) Charging/discharging polarization curves for conventional and urea-assisted ZABs. (f) Galvanostatic charging curves of urea-assisted and conventional ZABs at different current densities. (g) Urea elimination rates for the CoNi@NCNTs-LDH/CC based urea-assisted ZAB at different current densities. (h) Cycle performance of the urea-assisted and conventional ZABs at 10 mA cm<sup>-2</sup>.

10 h of galvanostatic charging at different current densities. With the current density from 5 to 20 mA cm<sup>-2</sup>, the urea elimination rate ranges from 37.5 to 78.9 g m<sup>-2</sup> h<sup>-1</sup> (Fig. 8g). It can be found that the urea elimination rates of urea-assisted ZAB would be higher at a larger current density. However, it is inevitable that there would be the competing OER at large current density, which in turn would lead to the decrease of Faraday efficiency of UOR. Then, in order to evaluate the energy conversion efficiency and cycling stability of the urea-assisted ZAB based on CoNi@NCNTs-LDH/CC, the cycle measurements were performed at 10 mA cm<sup>-2</sup>. As shown in Fig. 8h, the urea-assisted ZAB assembled with CoNi@NCNTs-LDH/CC shows a smaller voltage gap (0.43 V) with a higher energy conversion efficiency (74.6 %), which is significantly superior to the conventional rechargeable ZAB (0.57 V, 69.2 %). The results just demonstrate that prepared CoNi@NCNTs-LDH/CC has promising ORR-UOR bifunctional activity, and the assembled urea-assisted ZAB based on CoNi@NCNTs-LDH/CC displays efficient charging capacity due to the more dynamic favorable UOR reaction, which improves the overall energy conversion efficiency of ZAB devices.

In addition, after the cycling measurements at 10 mA cm<sup>-2</sup> for 350 h, the charge and discharge potentials can keep stable without evident decay for both urea-assisted and conventional ZAB, manifesting the desirable charge-discharge durability of actual ZAB device based on CoNi@NCNTs-LDH/CC.

#### 3.4. Urea-assisted water splitting driven by urea-assisted ZABs

Due to the lower overpotential of the UOR than OER, coupling the UOR with HER is an attractive technique for both wastewater treatment and efficient H<sub>2</sub> production. In view of the efficient UOR performance of CoNi@NCNTs-LDH/CC, a two-electrode water electrolyzer device was constructed with the CoNi@NCNTs-LDH/CC directly as the anode and Pt/C-CC as the cathode. As displayed in Fig. 9a, the high current density can be achieved at an ultra-low potential in the urea-assisted water splitting system, and the applied voltage is reduced by about 0.3 V compared to that of the conventional overall water splitting system at the current density of 50 mA cm<sup>-2</sup>, which manifests the more efficient



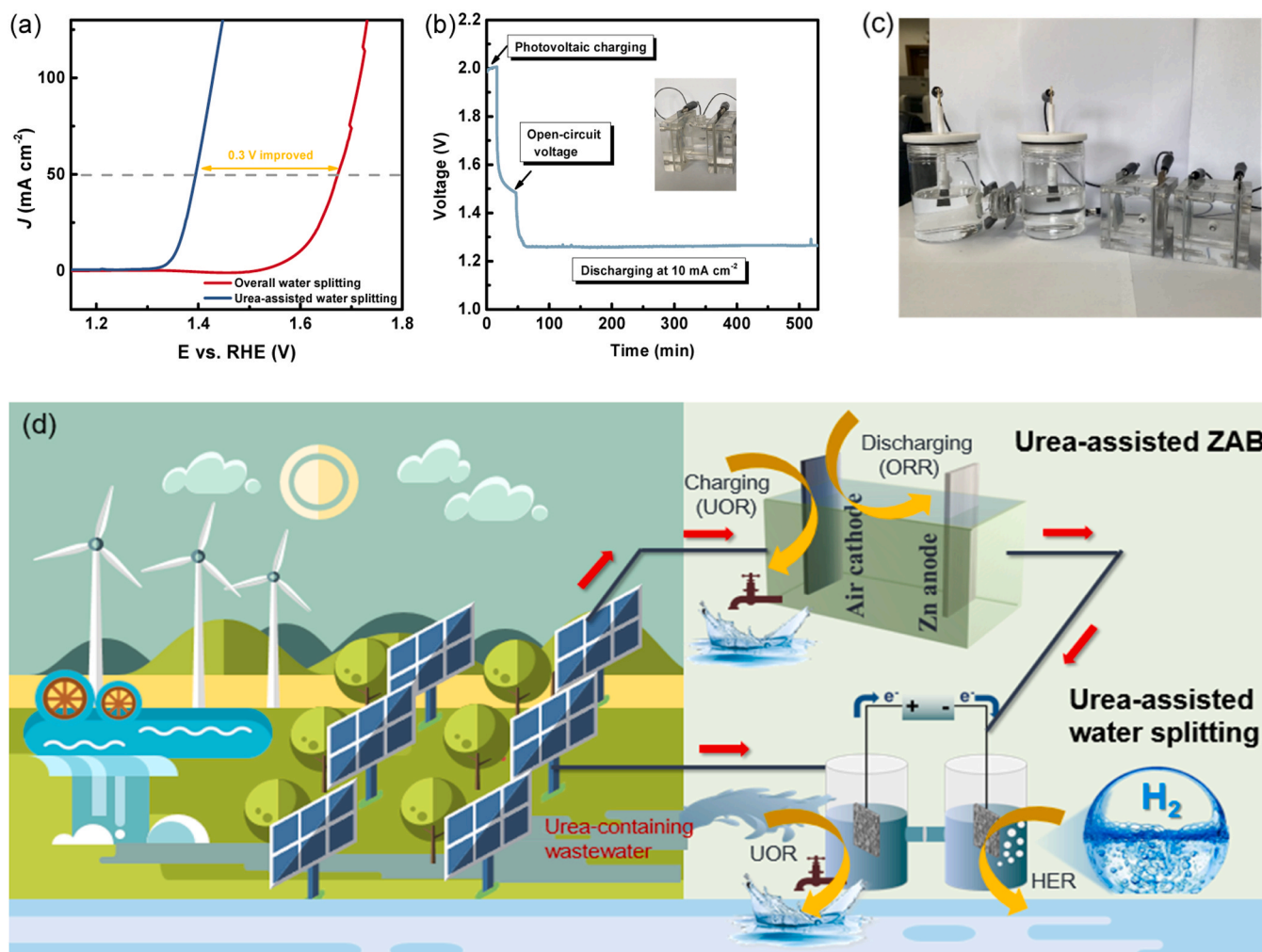


**Fig. 9.** (a) Polarization curves for urea-assisted water electrolysis. (b) The charging and subsequent discharging of the urea-assisted ZAB powered by a silicon solar cell. (c) Photo of the urea-assisted water splitting device driven by urea-assisted ZABs. (d) Schematic illustration of the novel urea-assisted ZAB as a transfer station between renewable energy and hydrogen.

## H<sub>2</sub> generation.

Considering the excellent charge-discharge efficiency and sewage treatment potential of the urea-assisted ZAB system, it is further used as an energy transfer station for intermittent renewable energy storage and continuous power supply for electrolytic water. As shown in Fig. 9b, after being charged by sustainable solar charging, the assembled ZAB displays an OCV of approximately 1.48 V, and the output voltage is stable at a current density of 10 mA cm<sup>-2</sup>. It confirms the significant sustainable energy conversion capability of the urea-assisted ZAB in a practical energy conversion configuration (Fig. 9c). And after storing the energy charged by the solar cell, the urea-assisted ZAB then discharges to provide electricity to drive the urea-assisted water splitting for uninterrupted H<sub>2</sub> production, when there is insufficient light. The H<sub>2</sub> production from urea-assisted water splitting driven by urea-assisted ZABs was measured using the water-gas displacing instrument. There is a linear relationship that can be observed for measured H<sub>2</sub> volumes versus times (Fig. S21), exhibiting high-efficient water splitting performance, which demonstrates the robust practical operation stability of the assembled urea-assisted water splitting systems driven by urea-assisted ZABs.

Therefore, based on the efficient energy conversion characteristics of the urea-assisted ZAB, it shows potential for application in a modern high value-added agricultural system, as depicted in Fig. 9d. For some photosensitive crops, long-term light growth conditions are not required, and the photovoltaic panels are installed next to crops to

achieve full utilization of light energy. During the day, photovoltaic solar cells convert solar energy into electricity and charge the urea-assisted ZABs to store electricity, simultaneously achieving the degradation of agricultural wastewater containing urea sewage. During the night, the urea-assisted ZABs further release electricity to drive the urea-assisted water splitting to achieve uninterrupted H<sub>2</sub> production using sustainable energy sources, while also simultaneously achieving the purification of agricultural wastewater. Therefore, with the urea-assisted ZAB as the high energy conversion efficiency transfer station, the efficient H<sub>2</sub> generation from agricultural wastewater can be realized by only utilizing sustainable energy sources, such as wind and solar energy, simultaneously achieving the purification of wastewater.

## 4. Conclusion

In conclusion, a binary-site "leaf-branch" catalyst of CoNi@NCNTs-LDH/CC is reported, where spatially separated branches and leaves serve as the main active sites for ORR and UOR, respectively. The presence of a built-in electric field promotes the directional movement and aggregation of UOR and ORR reactants to their respective reaction sites. The urea-assisted rechargeable ZAB based on CoNi@NCNTs-LDH/CC maintains excellent discharging property, and displays significantly reduced charging voltage, thus acquiring a higher energy conversion efficiency of 74.6 % than that of traditional ORR and OER-coupled ZAB. This work not only provides new ideas for the design of bifunctional



catalysts, but also offers potential opportunities for the development of novel electrochemical energy storage devices with high energy conversion efficiency and additional applications.

### CRediT authorship contribution statement

**Lei Wang:** Investigation. **Hao-Yu Wang:** Investigation. **Jin-Tao Ren:** Writing – review & editing, Investigation, Funding acquisition. **Wen-Wen Tian:** Writing – original draft, Methodology, Investigation, Conceptualization. **Zhong-Yong Yuan:** Writing – review & editing, Supervision, Project administration, Funding acquisition.

### Declaration of Competing Interest

The authors declare that they have no known competing financial interests or personal relationships that could have appeared to influence the work reported in this paper.

### Data availability

Data will be made available on request.

### Acknowledgments

This work was supported by the National Natural Science Foundation of China (22179065, 22105108), and China Postdoctoral Science Foundation (2020M680860).

### Appendix A. Supporting information

Supplementary data associated with this article can be found in the online version at doi:10.1016/j.apcatb.2024.124115.

### References

- [1] D. Yan, C. Mebrahtu, S. Wang, R. Palkovits, Innovative electrochemical strategies for hydrogen production: from electricity input to electricity output, *Angew. Chem. Int. Ed.* 62 (2023) e202214333.
- [2] H. Liu, S. Shi, Z. Wang, Y. Han, W. Huang, Recent advances in metal-gas batteries with carbon-based nonprecious metal catalysts, *Small* 18 (2021) 2103747.
- [3] M. Wu, G. Zhang, H. Yang, X. Liu, M. Dubois, M.A. Gauthier, S. Sun, Aqueous Zn-based rechargeable batteries: recent progress and future perspectives, *InfoMat* 4 (2021) e12265.
- [4] N. Borchers, S. Clark, B. Horstmann, K. Jayasayee, M. Juel, P. Stevens, Innovative zinc-based batteries, *J. Power Source* 484 (2021) 229309.
- [5] X.-W. Lv, Z. Wang, Z. Lai, Y. Liu, T. Ma, J. Geng, Z.-Y. Yuan, Rechargeable Zn-air batteries: advances, challenges and prospects, *Small* 19 (2023) 2306396.
- [6] J. Balamurugan, T.T. Nguyen, D.H. Kim, N.H. Kim, J.H. Lee, 3D nickel molybdenum oxyhydride ( $\text{Ni}_{1-x}\text{Mo}_x\text{OSe}$ ) nanoarchitectures as advanced multifunctional catalyst for Zn-air batteries and water splitting, *Appl. Catal. B: Environ.* 286 (2021) 119909.
- [7] L. Yan, Y. Xu, P. Chen, S. Zhang, H. Jiang, L. Yang, Y. Wang, L. Zhang, J. Shen, X. Zhao, L. Wang, A freestanding 3D heterostructure film stitched by MOF-derived carbon nanotube microsphere superstructure and reduced graphene oxide sheets: a superior multifunctional electrode for overall water splitting and Zn-air batteries, *Adv. Mater.* 32 (2020) 2003313.
- [8] W. Cheng, P. Yuan, Z. Lv, Y. Guo, Y. Qiao, X. Xue, X. Liu, W. Bai, K. Wang, Q. Xu, J. Zhang, Boosting defective carbon by anchoring well-defined atomically dispersed metal-N<sub>4</sub> sites for ORR, OER, and Zn-air batteries, *Appl. Catal. B: Environ.* 260 (2020) 118198.
- [9] H. Jiang, J. Xia, L. Jiao, X. Meng, P. Wang, C.-S. Lee, W. Zhang, Ni single atoms anchored on N-doped carbon nanosheets as bifunctional electrocatalysts for Urea-assisted rechargeable Zn-air batteries, *Appl. Catal. B: Environ.* 310 (2022) 121352.
- [10] Y. Feng, Q. Shi, J. Lin, E. Chai, X. Zhang, Z. Liu, L. Jiao, Y. Wang, Decoupled electrochemical hydrazine “splitting” via a rechargeable Zn-hydrazine battery, *Adv. Mater.* 34 (2022) 2207747.
- [11] T. Wang, X. Cao, L. Jiao, Progress in hydrogen production coupled with electrochemical oxidation of small molecules, *Angew. Chem. Int. Ed.* 61 (2022) e202213328.
- [12] H. Sun, L. Li, H.-C. Chen, D. Duan, M. Humayun, Y. Qiu, X. Zhang, X. Ao, Y. Wu, Y. Pang, K. Huo, C. Wang, Y. Xiong, Highly efficient overall urea electrolysis via single-atomically active centers on layered double hydroxide, *Sci. Bull.* 67 (2022) 1763–1775.
- [13] R.K. Singh, K. Rajavelu, M. Montag, A. Schechter, Advances in catalytic electrooxidation of urea: a review, *Energy Tech.* 9 (2021) 2100017.
- [14] J.-T. Ren, Y.-D. Ying, Y.-P. Liu, W. Li, Z.-Y. Yuan, Charge redistribution caused by sulfur doping of bimetal FeCo phosphides supported on heteroatoms-doped graphene for Zn-air batteries with stable cycling, *J. Energy Chem.* 71 (2022) 619–630.
- [15] W.-W. Tian, J.-T. Ren, Z.-Y. Yuan, In-situ cobalt-nickel alloy catalyzed nitrogen-doped carbon nanotube arrays as superior freestanding air electrodes for flexible zinc-air and aluminum-air batteries, *Appl. Catal. B: Environ.* 317 (2022) 121764.
- [16] Z. Lu, H. Yang, G. Qi, Q. Liu, L. Feng, H. Zhang, J. Luo, X. Liu, Efficient and stable pH-universal water electrolysis catalyzed by N-doped hollow carbon confined RuIrO<sub>x</sub> nanocrystals, *Small* (2023) 2308841.
- [17] C. Kim, F. Dionigi, V. Beermann, X. Wang, T. Möller, P. Strasser, Alloy nanocatalysts for the electrochemical oxygen reduction (ORR) and the direct electrochemical carbon dioxide reduction reaction (CO<sub>2</sub>RR), *Adv. Mater.* 31 (2018) 1805617.
- [18] H.-Y. Wang, C.-C. Weng, Z.-Y. Yuan, Insights into efficient transition metal-nitrogen/carbon oxygen reduction electrocatalysts, *J. Energy Chem.* 56 (2021) 470–485.
- [19] X. Xu, Z. Xia, X. Zhang, R. Sun, X. Sun, H. Li, C. Wu, J. Wang, S. Wang, G. Sun, Atomically dispersed Fe-N-C derived from dual metal-organic frameworks as efficient oxygen reduction electrocatalysts in direct methanol fuel cells, *Appl. Catal. B: Environ.* 259 (2019) 118042.
- [20] N.A. Galiote, F.E.R. Oliveira, F.H.B. Lima, FeCo-N-C oxygen reduction electrocatalysts: Activity of the different compounds produced during the synthesis via pyrolysis, *Appl. Catal. B: Environ.* 253 (2019) 300–308.
- [21] C.C. Weng, J.T. Ren, H.Y. Wang, X.W. Li, Y.J. Song, Y.S. Wang, L. Chen, W.W. Tian, Z.Y. Yuan, Triple-phase oxygen electrocatalysis of hollow spherical structures for rechargeable Zn-air batteries, *Appl. Catal. B: Environ.* 307 (2022) 121190.
- [22] Q. Zhang, K. Lian, Q. Liu, G. Qi, S. Zhang, J. Luo, X. Liu, High entropy alloy nanoparticles as efficient catalysts for alkaline overall seawater splitting and Zn-air batteries, *J. Colloid Interface Sci.* 646 (2023) 844–854.
- [23] J. Ding, H. Yang, H. Zhang, Z. Wang, Q. Liu, L. Feng, G. Hu, J. Luo, X. Liu, Dealloyed NiTiZrAg as an efficient electrocatalyst for hydrogen evolution in alkaline seawater, *Int. J. Hydrog. Energy* 53 (2024) 318–324.
- [24] J. Yu, F. Yu, M.-F. Yuen, C. Wang, Two-dimensional layered double hydroxides as a platform for electrocatalytic oxygen evolution, *J. Mater. Chem. A* 9 (2021) 9389–9430.
- [25] J.-T. Ren, L. Chen, H.-Y. Wang, W.-W. Tian, X.-L. Song, Q.-H. Kong, Z.-Y. Yuan, Synergistic activation of crystalline Ni<sub>2</sub>P and amorphous NiMoO<sub>4</sub> for efficient water splitting at high current densities, *ACS Catal.* 13 (2023) 9792–9805.
- [26] H. Liu, S. Zhu, Z. Cui, Z. Li, S. Wu, Y. Liang, Ni<sub>2</sub>P nanoflakes for the high-performance urea oxidation reaction: linking active sites to a UOR mechanism, *Nanoscale* 13 (2021) 1759–1769.
- [27] X. Wang, J.P. Li, Y. Duan, J. Li, H. Wang, X. Yang, M. Gong, Electrochemical urea oxidation in different environment: from mechanism to devices, *ChemCatChem* 14 (2022) e202101906.
- [28] R. Liu, Y. Wang, S. Sun, C. Chen, X. Wu, CoNi layered double hydroxide anchored on N-doped carbon coated carbon nanotubes network with 3D Core-shell structure for all-solid-state supercapacitors, *J. Electroanal. Chem.* 878 (2020) 114571.
- [29] C. Chen, H. Su, L.-N. Lu, Y.-S. Hong, Y. Chen, K. Xiao, T. Ouyang, Y. Qin, Z.-Q. Liu, Interfacial spinel NiCo<sub>2</sub>O<sub>4</sub> and NiCo alloy derived N-doped carbon nanotubes for enhanced oxygen electrocatalysis, *Chem. Eng. J.* 408 (2021) 127814.
- [30] W.-W. Tian, J.-T. Ren, X.-W. Lv, Z.-Y. Yuan, A “gas-breathing” integrated air diffusion electrode design with improved oxygen utilization efficiency for high-performance Zn-air batteries, *Chem. Eng. J.* 431 (2022) 133210.
- [31] D. Wu, H. Huang, M. Haq, L. Zhang, J. Feng, A. Wang, Lignin-derived iron carbide/Mn, N, S-codoped carbon nanotubes as a high-efficiency catalyst for synergistically enhanced oxygen reduction reaction and rechargeable zinc-air battery, *J. Colloid Interface Sci.* 647 (2023) 1–11.
- [32] Y. Liu, L. Yang, B. Xie, N. Zhao, L. Yang, F. Zhan, Q. Pan, J. Han, X. Wang, J. Liu, J. Li, Y. Yang, Ultrathin Co<sub>3</sub>O<sub>4</sub> nanosheet clusters anchored on nitrogen doped carbon nanotubes/3D graphene as binder-free cathodes for Al-air battery, *Chem. Eng. J.* 381 (2020) 122681.
- [33] L. Liu, D. Wu, L. Zhang, J. Feng, A. Wang, FeCo alloy entrapped in N-doped graphitic carbon nanotubes-onnanosheets prepared by coordination-induced pyrolysis for oxygen reduction reaction and rechargeable Zn-air battery, *J. Colloid Interface Sci.* 639 (2023) 424–433.
- [34] F. Zhu, W. Liu, Y. Liu, W. Shi, Construction of porous interface on CNTs@NiCo-LDH core-shell nanotube arrays for supercapacitor applications, *Chem. Eng. J.* 383 (2020) 123150.
- [35] L. Zhang, L. Liu, J. Feng, A. Wang, Methanol-induced assembly and pyrolysis preparation of three-dimensional N-doped interconnected open carbon cages supported FeNb<sub>2</sub>O<sub>6</sub> nanoparticles for boosting oxygen reduction reaction and Zn-air battery, *J. Colloid Interface Sci.* 661 (2024) 102–112.
- [36] D. Xie, D. Yu, Y. Hao, S. Han, G. Li, X. Wu, F. Hu, L. Li, H.Y. Chen, Y.F. Liao, S. Peng, Dual-active sites engineering of N-doped hollow carbon nanocubes confining bimetal alloys as bifunctional oxygen electrocatalysts for flexible metal-air batteries, *Small* 17 (2021) 2007239.
- [37] W.-W. Tian, Y.-D. Ying, J.-T. Ren, Z.-Y. Yuan, A trifunctional Co<sub>0.85</sub>Se/NC collaborated electrocatalyst enables a self-powered energy system for uninterrupted H<sub>2</sub> production, *J. Mater. Chem. A* 11 (2023) 8024–8037.
- [38] L. Wang, T. Du, J. Cheng, X. Xie, B. Yang, M. Li, Enhanced activity of urea electrooxidation on nickel catalysts supported on tungsten carbides/carbon nanotubes, *J. Power Source* 280 (2015) 550–554.
- [39] Z. Xu, Q. Chen, Q. Chen, P. Wang, J. Wang, C. Guo, X. Qiu, X. Han, J. Hao, Interface enables faster surface reconstruction in a heterostructured Co-Ni-S electrocatalyst towards efficient urea oxidation, *J. Mater. Chem. A* 10 (2022) 24137–24146.



- [40] K. He, T. TadesseTsega, X. Liu, J. Zai, X.H. Li, X. Liu, W. Li, N. Ali, X. Qian, Utilizing the space-charge region of the FeNi-LDH/CoP p-n Junction to Promote Performance in Oxygen Evolution Electrocatalysis, *Angew. Chem. Int. Ed.* 58 (2019) 11903–11909.
- [41] L. Zhai, X. She, L. Zhuang, Y. Li, R. Ding, X. Guo, Y. Zhang, Y. Zhu, K. Xu, H. Fan, S. Lau, Modulating built-in electric field via variable oxygen affinity for robust hydrogen evolution reaction in neutral media, *Angew. Chem. Int. Ed.* 61 (2022) e202116057.
- [42] C. He, Q. Liu, H. Wang, C. Xia, F.M. Li, W. Guo, B.Y. Xia, Regulating reversible oxygen electrocatalysis by built-in electric field of heterojunction electrocatalyst with modified d-band, *Small* 19 (2023) 2207474.
- [43] X. Zhao, K. Tang, C. Lee, C.F. Du, H. Yu, X. Wang, W. Qi, Q. Ye, Q. Yan, Promoting the water-reduction kinetics and alkali tolerance of MoNi<sub>4</sub> nanocrystals via a Mo<sub>2</sub>TiC<sub>2</sub>T<sub>3</sub> induced built-in electric field, *Small* 18 (2022).
- [44] H. Lee, O. Gwon, K. Choi, L. Zhang, J. Zhou, J. Park, J.-W. Yoo, J.-Q. Wang, J. H. Lee, G. Kim, Enhancing bifunctional electrocatalytic activities via metal d-band center lift induced by oxygen vacancy on the subsurface of perovskites, *ACS Catal.* 10 (2020) 4664–4670.
- [45] X.-R. Wang, J.-Y. Liu, Z.-W. Liu, W.-C. Wang, J. Luo, X.-P. Han, X.-W. Du, S.-Z. Qiao, J. Yang, Identifying the key role of pyridinic-N-Co bonding in synergistic electrocatalysis for reversible ORR/OER, *Adv. Mater.* 30 (2018) 1800005.
- [46] Y.-N. Chen, X. Zhang, H. Cui, X. Zhang, Z. Xie, X.-G. Wang, M. Jiao, Z. Zhou, Synergistic electrocatalytic oxygen reduction reactions of Pd/B<sub>4</sub>C for ultra-stable Zn-air batteries, *Energy Storage Mater.* 15 (2018) 226–233.
- [47] J.-C. Li, X. Qin, P.-X. Hou, M. Cheng, C. Shi, C. Liu, H.-M. Cheng, M. Shao, Identification of active sites in nitrogen and sulfur co-doped carbon-based oxygen reduction catalysts, *Carbon* 147 (2019) 303–311.
- [48] H. Qin, Y. Ye, J. Li, W. Jia, S. Zheng, X. Cao, G. Lin, L. Jiao, Synergistic engineering of doping and vacancy in Ni(OH)<sub>2</sub> to boost urea electrooxidation, *Adv. Funct. Mater.* 33 (2022) 2209698.
- [49] L. Zhang, L. Wang, H. Lin, Y. Liu, J. Ye, Y. Wen, A. Chen, L. Wang, F. Ni, Z. Zhou, S. Sun, Y. Li, B. Zhang, H. Peng, A lattice-oxygen-involved reaction pathway to boost urea oxidation, *Angew. Chem. Int. Ed.* 58 (2019) 16820–16825.
- [50] L. Chen, L. Wang, J.T. Ren, H.Y. Wang, W.W. Tian, M.L. Sun, Z.Y. Yuan, Artificial heterointerfaces with regulated charge distribution of Ni active sites for urea oxidation reaction, *Small Methods* 8 (2024) 2400108.